

Retrieving Freeze/Thaw Surface State from CYGNSS Measurements

H. Carreno-Luengo, *Senior Member, IEEE*, and C.S. Ruf, *Fellow, IEEE*

Abstract—Freeze/Thaw (F/T) surface state retrieval is important to further understand hydrological patterns and climate change. This paper investigates the use of Earth-reflected Global Positioning System (GPS) L-band signals as collected by the National Aeronautics and Space Administration NASA’s CYclone Global Navigation Satellite System (CYGNSS) mission for F/T surface state retrieval over a target area in South America, covering the Andes Mountains and the Argentinian Pampas. In the study, CYGNSS’s responsiveness to changes in surface permittivity is leveraged to detect transitions of F/T surface state, at an improved spatio-temporal sampling as compared to traditional Remote Sensing missions. A Seasonal-Threshold Algorithm (STA) is developed and validated using surface temperature data as provided by the European Centre for Medium-Range Weather Forecast (ECMWF) ERA5-Land numerical reanalysis model. Then, the monthly evolution of CYGNSS-derived F/T surface state maps is evaluated and an inter-comparison with the Soil Moisture Active Passive (SMAP) F/T data product is performed.

Index Terms—GNSS-R, CYGNSS, Freeze/Thaw retrieval, SMAP, ECMWF ERA5-Land, Andes Mountains

I. INTRODUCTION

THE spatio-temporal variability of F/T surface state is high over the cryosphere. It has a strong influence in climate, biogeochemical processes, and seasonal surface energy exchange [1], and it determines vegetation net primary production and Net Ecosystem CO₂ Exchange (NEE) with the atmosphere [2]. Additionally, it is important to highlight that more than one third of the Earth’s land surface is covered by seasonal or permanent soil frost. Many agricultural, engineering, and environmental issues are affected by F/T surface state [3].

Detecting highly dynamic F/T transitions at large scales requires spaceborne Remote Sensing observations. Landscape F/T processes are significantly heterogeneous [4]. Synthetic Aperture Radar (SAR) missions generate high spatial resolution (~ 100 m) but low temporal resolution (~ 7-14 days) F/T products, which prevents monitoring F/T transitions with the required spatio-temporal resolution. On the other hand, microwave radiometry missions provide high temporal

resolution (~ 3 days) but low spatial resolution (~ 25 km), which prevents observing the landscape processes that directly affect F/T surface state [5-7]. Currently, there is no way to simultaneously monitor F/T surface state globally, at appropriate spatial and temporal scales.

Brightness temperature, backscatter, and forward-scatter vary due to changes in the surface permittivity when water changes its state (liquid or solid), but also they are a function of a wide range of surface and instrument properties. The change in the surface permittivity due to F/T surface state transitions and how this phenomenon impacts observed surface reflectivity form the corner stone of the formulation presented in this study. The surface permittivity changes when the temperature goes from below 0 °C to above 0 °C. This process leads to changes in the surface reflectivity. This is the fundamental element of F/T surface state change detection. The permittivity of a thawed soil is much higher than that of a frozen soil.

Spaceborne microwave radiometry and SAR missions-derived measurements at several frequencies have been used to detect melt onset [8,9] and landscape F/T state [10-15]. In particular, microwave observations at L-band have demonstrated the ability to detect F/T surface state because of the following reasons: a) a strong sensitivity to surface permittivity, which is influenced by the phase of water; and b) a higher penetration depth through the vegetation and into soil surface than at higher frequencies (starting at C-band) from sensors such as e.g. the Advanced Microwave Scanning Radiometer-Earth Observing System (AMSR-E) [16]. Ground-based L-band radiometers have been used to detect F/T surface state [17-19] and several algorithms have been adapted to the Soil Moisture and Ocean Salinity (SMOS) mission [20]. High resolution L-band data from Phased Array Type L-band Synthetic Aperture Radar (PALSAR) have been used to detect local scale variability in F/T surface state transitions [21,22]. The NASA (Satélite de Aplicaciones Científicas/D) SAC/D-Aquarius mission pioneered large-scale L-band radar response to F/T surface state with coarse spatial (~ 100 km) and temporal (weekly) resolutions [23]. After the failure of the SMAP radar, the science team developed a new F/T surface state product

This research was supported in part by the NASA Science Mission Directorate contract NNL13AQ00C with the University of Michigan. (Corresponding author: Hugo Carreno-Luengo).

Hugo Carreno-Luengo is with the Department of Climate and Space Sciences and Engineering, University of Michigan, Ann Arbor, MI 48109 USA (e-mail: carreno@umich.edu).

Christopher S. Ruf is with the Department of Climate and Space Sciences and Engineering, University of Michigan, Ann Arbor, MI 48109 USA, and also with the Department of Electrical Engineering and Computer Science, University of Michigan, Ann Arbor, MI 48109 USA (e-mail: cruf@umich.edu).

using L-band radiometer measurements [6].

Global Navigation Satellite Systems Reflectometry (GNSS-R) can be understood as an L-band passive multi-bistatic radar e.g. [24-29]. In principle, spaceborne GNSS-R sensors can provide global coverage and sampling of the Earth's surface over multiple tracks simultaneously. Several spaceborne experiments and missions have been deployed. CYGNSS is the first-ever operational mission [30], providing coverage over tropical latitudes $\sim [-40, 40]^\circ$. Earth-reflected GNSS signals have sensitivity to a wide variety of geophysical parameters, such as, e.g., Snow Water Equivalent (SWE) [31], Soil Moisture Content (SMC) [32-35], vegetation parameters [35,36], and inland water bodies [37,38].

More recently, some pioneering studies have shown a promising sensitivity to F/T surface state transitions over high latitude regions, including SMAP GNSS-R mode [34,39], and TechDemoSat-1 [40]; and also CYGNSS [41]. CYGNSS [30] was originally proposed for ocean surface winds speed estimation over tropical cyclones using reflected L1 GPS signals at Left Hand Circular Polarization (LHCP). CYGNSS enables observations of the Earth's surface along 32 tracks simultaneously. The unique sampling properties of CYGNSS could enable an improved understanding of F/T surface state dynamics. In this work, CYGNSS data are used to investigate the potential capability of GNSS-R to determine the F/T surface state over the Andes Mountains. The generated theoretical and experimental capabilities developed here could be applied to high inclination GNSS-R missions (Spire CubeSats series and HydroGNSS), in order to better resolve spatial patterns and temporal dynamics with an improved spatio-temporal sampling as compared to traditional Remote Sensing missions. The F/T changes of seasonally frozen ground are an important indicator of climate change and contributor to global methane distributions.

II. FREEZE/THAW DETECTION WITH GNSS-R: THEORETICAL BACKGROUND

The CYGNSS-derived surface reflectivity Γ is directly related to the square modulus of the cross-polarization Fresnel reflection coefficient R_{cross} . This can be theoretically expressed as follows:

$$R_{\text{cross}} = \frac{1}{2}(R_{\text{VV}} - R_{\text{HH}}) \quad (1)$$

where

$$R_{\text{VV}} = \frac{\varepsilon \cos \theta_i - \sqrt{\varepsilon - (\sin \theta_i)^2}}{\varepsilon \cos \theta_i + \sqrt{\varepsilon - (\sin \theta_i)^2}} \quad (2)$$

and

$$R_{\text{HH}} = \frac{\cos \theta_i - \sqrt{\varepsilon - (\sin \theta_i)^2}}{\cos \theta_i + \sqrt{\varepsilon - (\sin \theta_i)^2}} \quad (3)$$

are the vertical V-pol and horizontal H-pol Fresnel reflection coefficients, respectively. ε is the complex relative permittivity

of the reflecting medium, and θ_i is the incidence angle. For angles larger than $\theta_i \sim 50^\circ$, there is a significant reduction in the reflection coefficient, while it remains roughly constant in the range $\theta_i = [0, 50]^\circ$ [42].

The complex relative permittivity ε describes the electrical properties of the reflecting medium. It can be analytically computed as follows [43]:

$$\varepsilon = \varepsilon' + i\varepsilon'' \quad (4)$$

where ε' is the dielectric constant, which is related with the speed of propagation, and ε'' is the so-called dielectric loss factor that is related with the attenuation rate of electromagnetic energy flow. It is highlighted that ε depends on the electromagnetic wavelength of the incident signal as well as on the internal components of the reflecting medium and their relative distribution.

The permittivity of a mixed medium of soil and water ε_s can be formulated as follows [41,44,45].

$$\varepsilon_s = 1 + \frac{\rho_b}{\rho_s}(\varepsilon_s^\alpha - 1) + m_v \varepsilon_{\text{fw}}^\alpha - m_v \quad (5)$$

where ρ_b is the bulk density, ρ_s is the solid density, and ε_s^α and $\varepsilon_{\text{fw}}^\alpha$ are the permittivity of the solid matter and pure water, respectively. α is the shape factor, and m_v is the total moisture.

In the case of frozen soil, the phase state of the water changes. The ice composition can be added to the permittivity model. The final permittivity of frozen soil can be expressed as follows [41,46]:

$$\varepsilon_{s,\text{frozen}} = V_s \varepsilon_s^\alpha + V_a \varepsilon_a^\alpha + V_{\text{fw}} \varepsilon_{\text{fw}}^\alpha + V_{\text{bw}} \varepsilon_{\text{bw}}^\alpha + V_i \varepsilon_i^\alpha \quad (6)$$

where V is the volume content of different components, and the subscripts s , a , fw , bw , and i are solid soil, air, free water, bound water, and ice, respectively.

The transition from thawed to frozen soil surface significantly decreases the permittivity. Consequently, R_{cross} decreases, which in turns reduces the surface reflectivity. This phenomenon is the fundamental basis of F/T surface state detection in this study.

III. DATASETS

A. Target Area

CYGNSS provides an unprecedented spatio-temporal sampling of the Earth's surface over tropical latitudes. The selected target area (Lat = $[-35, -28]^\circ$, Lon = $[-71, -67]^\circ$) includes a region of the Andes (Fig. 1) because permafrost takes place extensively over these high-altitude mountains [47]. In the northern Andes, permafrost can be detected above $\sim 5,000$ m. This lower limit gradually decreases down to $\sim 1,500$ m in Southern regions of Chile and Argentina. The total area affected by permafrost is $\sim 30,000$ km².

B. CYGNSS

CYGNSS Level 1 (L1) data from the version 3.0 (v3.0) Science Data Record [48,49], available at the Physical Oceanography Distributed Active Archive Center (PODAAC) [50], are used in this paper. L1 daily files are provided in



Fig. 1. Target area (Lat = [-35, -28] °, Lon = [-71, -67] °) in South America.

NetCDF format, each one with the required calibrated measurements and observables for each nominal specular point, so as to enable a wide variety of scientific studies over both land and ocean surfaces. Current v3.0 products incorporate real time monitoring of transmitted GPS power [48,49]. This provides an improvement as compared to v2.1, which assumes that transmitted GPS power is constant.

C. ECMWF ERA5-Land

ECMWF ERA5-Land describes a wide set of land variables over several decades with an improved resolution as compared to ERA5. It provides an accurate description of the past climate using synergistically physical models with global-scale measurements [51]. In this study, ERA5-Land reanalysis SMC and soil temperature data with hourly-frequency are selected as the reference, considering temperature in the first layer of the soil (0-7 cm) within the ECMWF Integrated Forecasting System (IFS). The surface is set at 0 cm in the IFS, the temperature is set at the middle of each layer, and heat transfer is estimated at the interfaces between them. The first layer of the soil is selected because both active and passive L-band observations (e.g. SMAP, SMOS, CYGNSS) have sensitivity to the top ~ 5 cm of soil [52].

D. SMAP

SMAP Enhanced L3 Radiometer Global and Northern Hemisphere Daily 9 km Equal-Area Scalable Earth (EASE)-Grid Freeze/Thaw State product is selected for this study. It provides a daily classification of F/T surface state derived from the SMAP L-band radiometer, over the global 9-km EASE 2.0 grid with a spatial resolution of ~ 20 km x 20 km [53]. To do so, the Backus–Gilbert technique is applied. This methodology enables the use of additional microwave radiometry data that are not available for the original product because the foundation measurements of brightness temperature are oversampled in the along-track direction.

IV. METHODOLOGY

A. Reflectivity Estimation

Analog Delay Doppler Maps (DDMs) are selected (*power_analog*), along with the required metadata, for estimation of the observables and interpretation of the results. *Power_analog* is the true power that would have been measured by an ideal (analog) power sensor. *Power_digital* is the power measured by the actual 2-bit sensor, which includes quantization effects. *Power_analog* (power after radiometric calibration) has been corrected for quantization effects. 1 year of data are considered from January to December 2019 to develop and to apply the retrieval algorithm. The equivalent “CYGNSS overall quality flag” over land surfaces is used to filter out the data, improving the quality of the observables (see Appendix for more information).

The delay bin resolution of the original 17 x 11 bins DDMs is 0.2552 GPS Coarse Acquisition (C/A) code chips, while the Doppler bin resolution is 500 Hz. After resampling, an interpolation [54] of the obtained 1,700 x 1,100 bins DDMs is applied to improve the accuracy, before performing the estimation of the reflectivity Γ . To do so, a spline method is used.

Earth-reflected delay waveforms $WF_{r,analog}$ are derived from the improved analog DDMs $\langle |Y_r(\tau, f)|^2 \rangle$ at zero Doppler frequency as:

$$WF_{r,analog} = \langle |Y_r(\tau, f = 0)|^2 \rangle \quad (7)$$

where τ is the delay of the signal from the transmitter to the receiver, and f is the Doppler shift of the electromagnetic reflected signal.

In this study, it is assumed that the received power is described by the reflection model given by the Friis transmission formula [55,56]. Γ is obtained as it follows [57]:

$$\Gamma = \frac{(4\pi)^2 (WF_{r,analog-Peak} - N)(R_r + R_t)^2}{\lambda^2 G_r G_t P_t} \quad (8)$$

where $WF_{r,analog-Peak}$ is the peak value of the analog delay waveform, N is the DDM noise floor, P_t is the transmitted power, G_t and G_r are the transmitter and the receiver antennas gains, R_t and R_r are the ranges from the transmitter and the receiver to the nominal specular point, respectively. $G_t P_t$ is the transmitter Equivalent Isotropically Radiated Power (EIRP), which is provided in the metadata files along with the other variables, except $WF_{r,analog-Peak}$ and N , which are calculated from the DDMs.

Over land surfaces, coherent and incoherent scattering terms contribute to the reflected power in a general scenario [58-67]. Some pioneering works have also shown the impact of topography and vegetation [68-71]. Since it is not practical to switch between reflectivity and Normalized Bistatic Radar Cross Section (NBRCS) with every DDM, a choice needs to be made to use one or the other.

The noise power floor is calculated as the mean value of the region of the DDM where there is no signal [72]. The delay separation between that region and the peak of DDM is at least

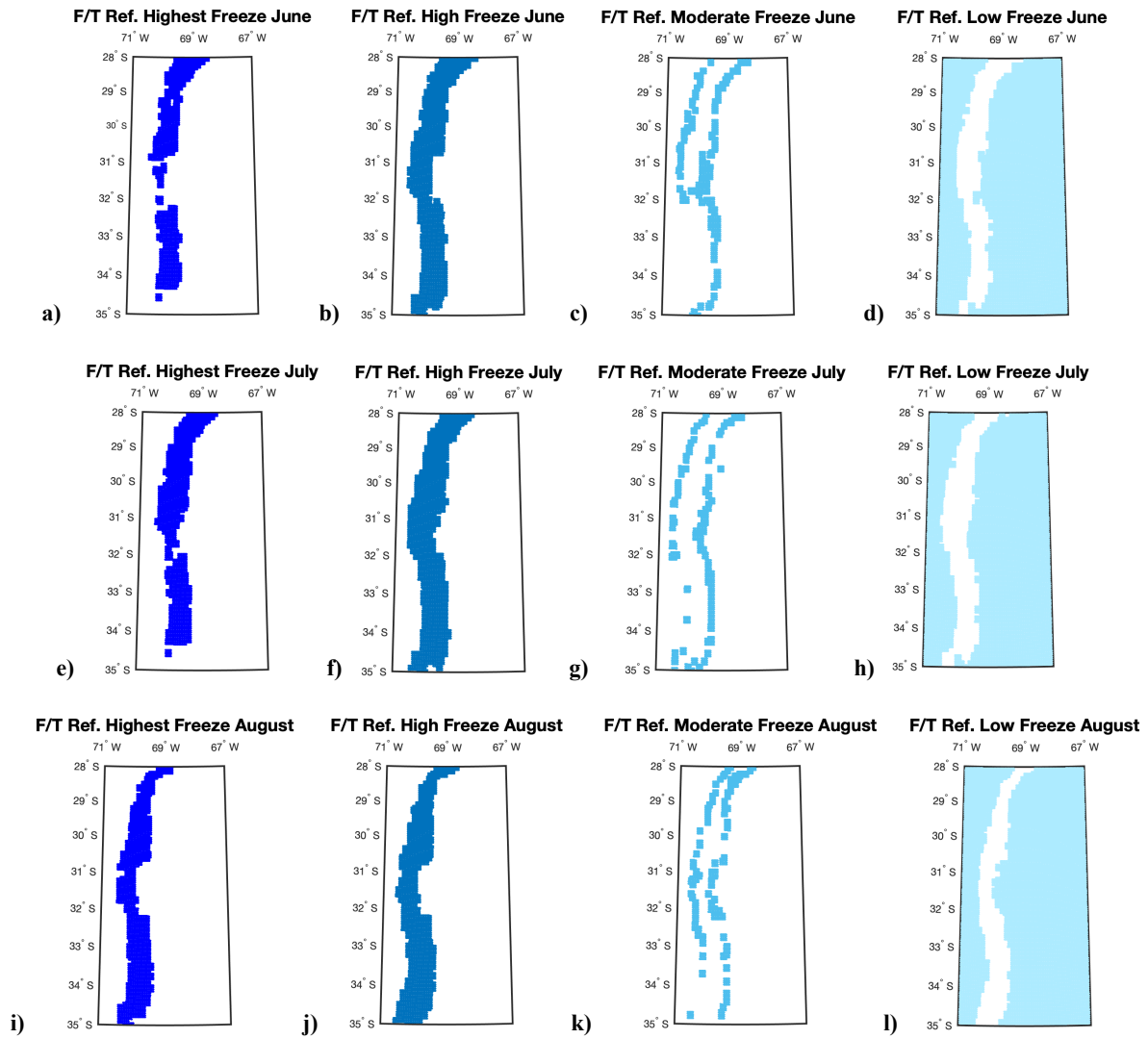


Fig. 2. Freeze surface state reference in June (a-d), July (e-h), and August (i-l) for several confidence levels: “highest” (a,e,i), “high” (b,f,j), “moderate” (c,g,k), and “low” (d,h,l). Different colors are associated with different confidence levels to help the interpretation of the results. Note: White means no data for this level.

0.75 C/A code chips. The estimation of Γ is not considered if this distance is below 0.75 C/A code chips.

B. Reference Freeze/Thaw Surface State

The assumed F/T surface state at a particular location in a particular month is derived from the population of hourly ERA5-Land temperatures, T_i , in that month. If the average of all values is $< -1^\circ\text{C}$, the state is defined as frozen. If the average is $> +1^\circ\text{C}$, the state is defined as thaw. The confidence in the state definition is derived from the statistical distribution of hourly samples in the month according to the following schedule:

- “Highest” freeze confidence: All hourly samples $T_i < -1^\circ\text{C}$
- “High” freeze confidence: All hourly samples $T_i < 1^\circ\text{C}$
- “Moderate” freeze confidence: Less than 10% of

hourly samples $T_i > 1^\circ\text{C}$

- “Low” freeze confidence: At least 10% of hourly samples $T_i > 1^\circ\text{C}$
- “Highest” thaw confidence: All hourly samples $T_i > 1^\circ\text{C}$
- “High” thaw confidence: All hourly samples $T_i > -1^\circ\text{C}$
- “Moderate” thaw confidence: Less than 10% of hourly samples $T_i < -1^\circ\text{C}$
- “Low” thaw confidence: At least 10% of hourly samples $T_i < -1^\circ\text{C}$

Examples of freeze state in Winter (June, July, August) and thaw state in Summer (January, February, March) with difference confidence levels are shown in Figs. 2,3 respectively,

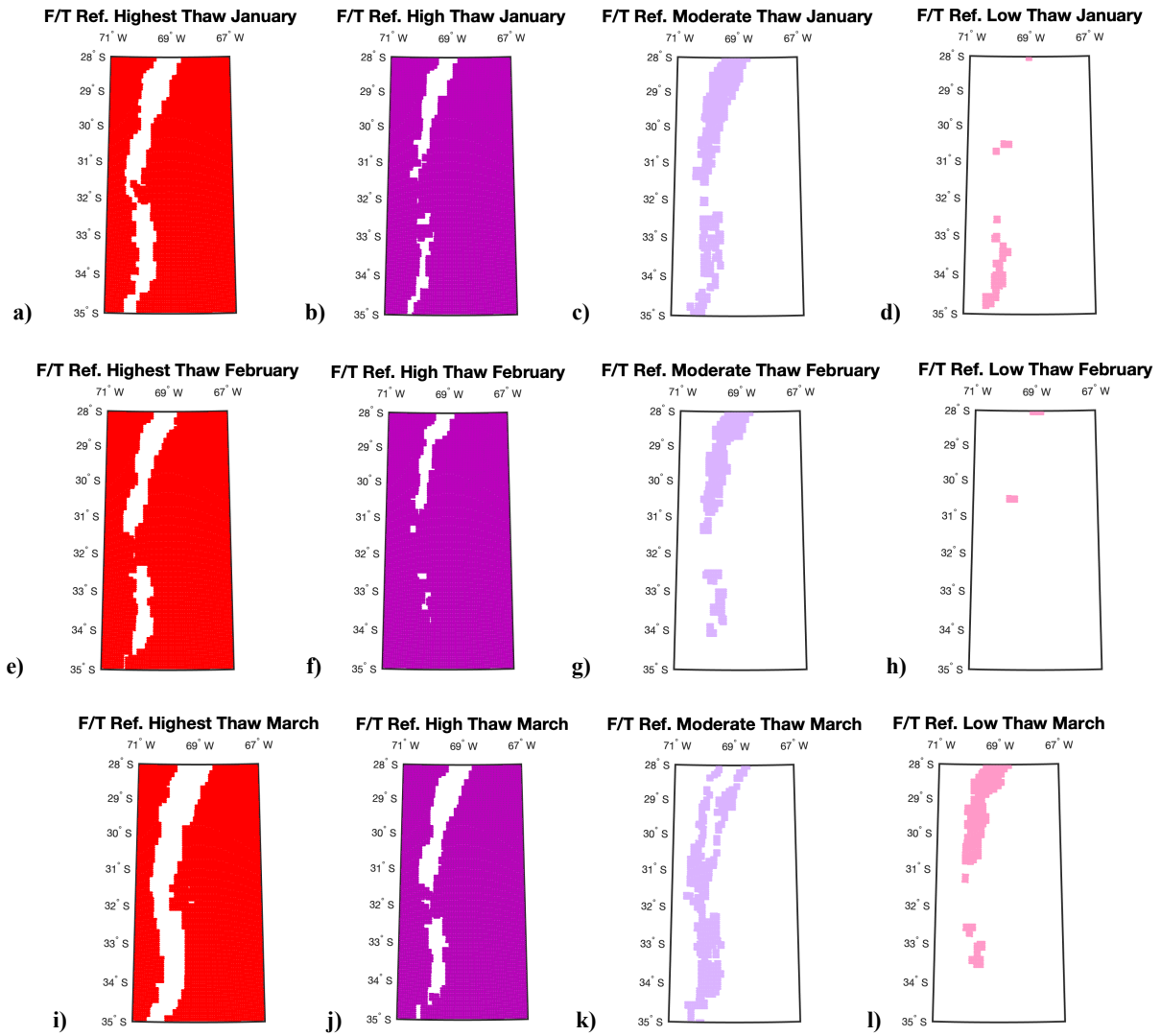


Fig. 3. Thaw surface state reference in January (a-d), February (e-h), and March (i-l) for several confidence levels: “highest” (a,e,i), “high” (b,f,j), “moderate” (c,g,k), and “low” (d,h,l). Different colors are associated with different confidence levels to help the interpretation of the results. Note: White means no data for this level.

for several months. In Winter, the “highest” confidence freeze state covers almost all the Andes. On the other hand, the “highest” confidence thaw state covers almost all the Pampas in Summer. The “moderate” confidence freeze and thaw states clearly cover the boundaries between the “high” and the “low” levels. Finally, the “low” freeze and thaw levels cover the “highest” thaw and freeze levels, respectively.

The schedule so defined provides the required scenario to properly evaluate the ability of CYGNSS for F/T retrieval, accounting for the different degrees of confidence on the F/T surface state reference. The “low” confidence levels can be clearly discarded because they cover regions with the “highest” confidence for the opposite surface state. On the other hand, “moderate” levels appear in the frontier, so in principle these areas are linked with a quite uncertain state. The performance of the “highest” and “high” levels are quantitatively analyzed based on the behavior of the retrieval algorithm hereafter defined.

C. Retrieval Algorithm

The F/T retrieval approach is based on the STA. This algorithm evaluates the relationship between time series of CYGNSS-derived reflectivity Γ (Fig. 4) and seasonal reference frozen and thawed states. For a measurement at time t , the seasonal scale factor $\Delta(t)$ is defined as follows [6]:

$$\Delta(t) = \frac{\Gamma(t) - \Gamma_{fr}}{\Gamma_{th} - \Gamma_{fr}} \quad (9)$$

where $\Gamma(t)$ is the reflectivity measurement estimated at time t , and Γ_{fr} & Γ_{th} are reflectivity measurements corresponding to frozen and thawed reference states, respectively. Different F/T surface states correspond to different observation times.

GNSS-R Earth’s surface sampling properties are pseudo-random. A specific gridding strategy is thus required. In this work, it is defined using CYGNSS’s sampling properties and it is applied also to data from ERA5-Land and SMAP.

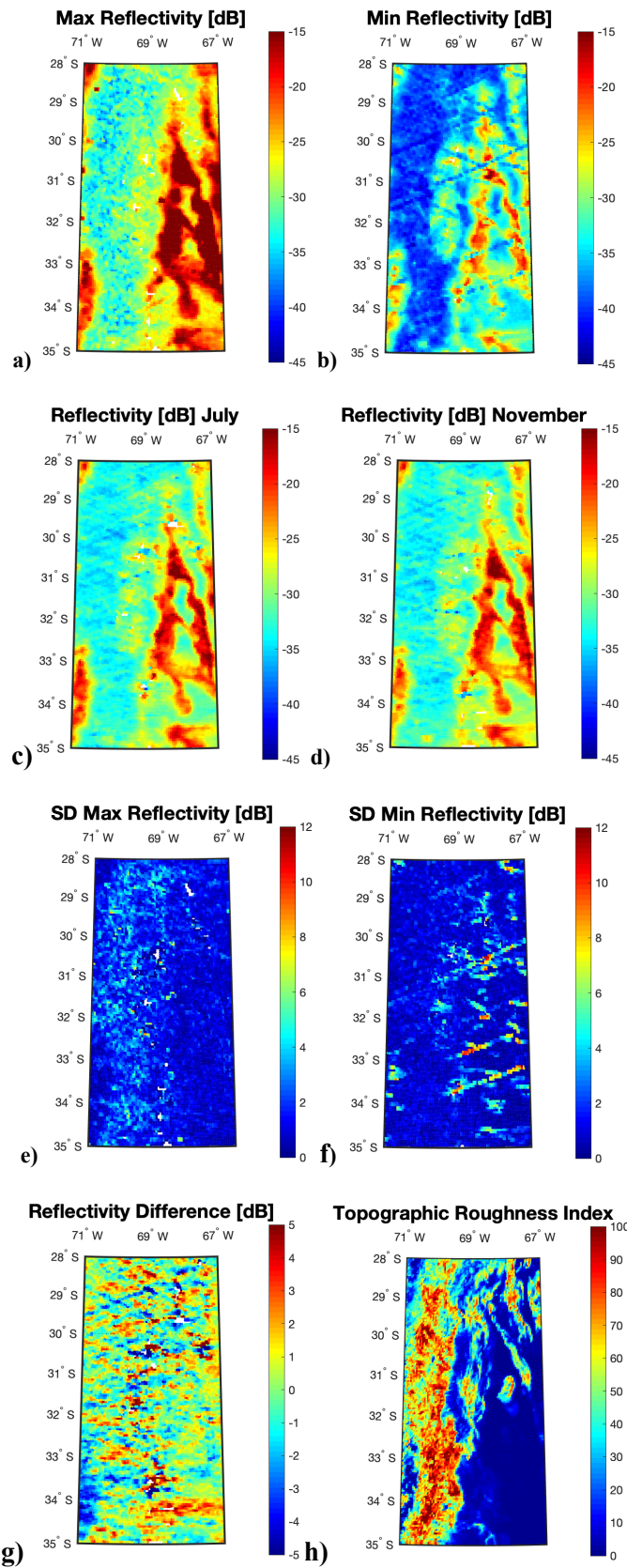


Fig 4. Averaged CYGNSS data over the target area: a) Maximum reflectivity Γ_{th} during Summer 2019, b) minimum reflectivity Γ_{fr} during Winter 2019, c) July reflectivity Γ , d) November reflectivity Γ , e) SD of the 5 largest values occurring in Summer, f) SD of the 5 smallest values occurring in Winter, g) November minus July reflectivity Γ , and h) Topographic Roughness Index [73].

The STA is evaluated for different sizes of the latitude/longitude grid ($0.1^\circ \times 0.1^\circ$, $0.05^\circ \times 0.05^\circ$, $0.001^\circ \times 0.001^\circ$), different number of measurements per pixel (5, 10, 20) and several temporal windows (1, 2, 3 months). Finally, a 0.05° by 0.05° grid is selected, and data are averaged using a moving window of 0.1° at steps of 0.05° . This selection provides a trade-off between the spatial resolution and the available number of measurements per pixel. The associated spatial resolution is ~ 10 km at equatorial latitudes.

Γ_{th} (Fig. 4a) is found by averaging the 5 largest values occurring in Summer, while Γ_{fr} (Fig. 4b) is found by averaging the 5 smallest values occurring in Winter. Overall, the Standard Deviation (SD) in the computation of both reference values is below ~ 1 dB (Figs. 4e,f). The variability of the maximum Γ values (Fig. 4e) is larger over areas with higher Topographic Roughness Index [73] (Fig. 4h) because of the larger temperature variability over high-altitude areas. On the other hand, the variability of the minimum Γ values (Fig. 4f) shows some few tracks with higher SD, probably because of the impact of non-geophysical effects [74,75]. The computation of both reference values does not depend on external reference datasets. The whole Winter and Summer sessions are the time periods over which Γ_{fr} and Γ_{th} are computed. Finally, it is worth to point out there is no impact of the SMC in the results (Figs. 5a,b).

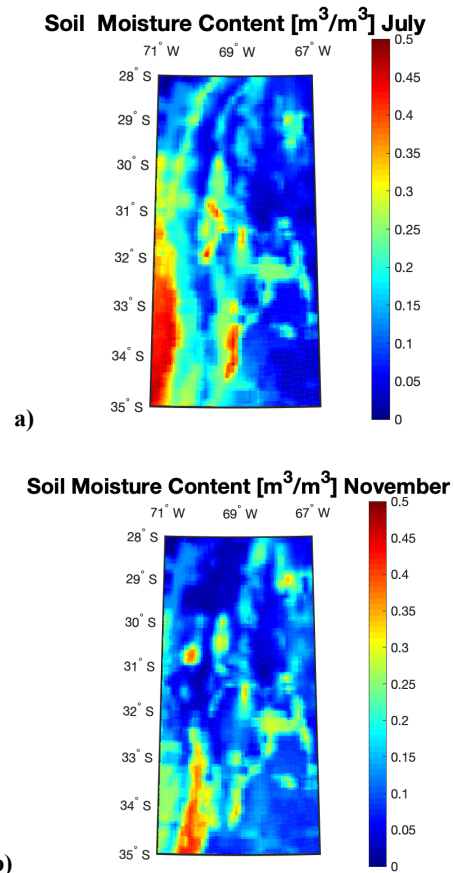


Fig. 5. a) July ERA5-Land SMC, and b) November ERA5-Land SMC.

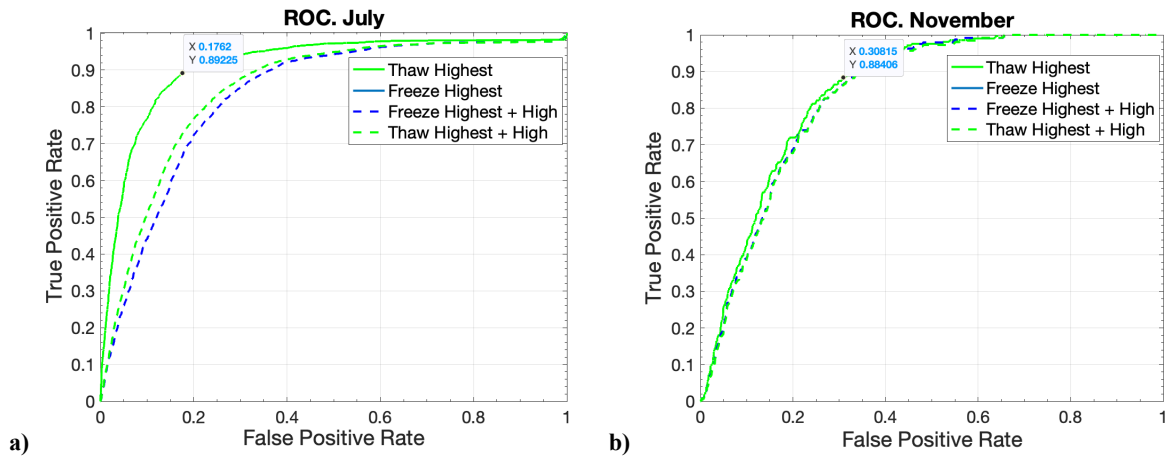


Fig. 6. ROC curves for “highest” and “high” freeze & thaw confidence levels: a) July and b) November.

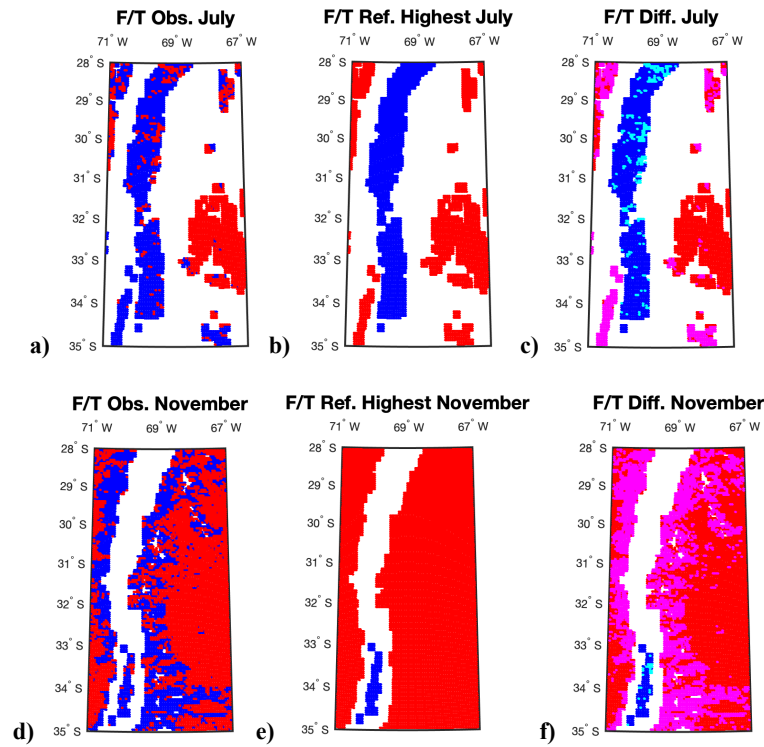


Fig. 7. Algorithm validation in July (a-c) and November (d-f). F/T maps (a,b,d,e) are blue when frozen and red when thawed. F/T maps derived from CYGNSS are labelled “Obs” (a,d). F/T maps derived from ERA5-Land with “highest” confidence are labelled “Ref” (b,e). Maps showing the difference between “Obs” and “Ref” are labelled “Diff”. “Diff” Maps are blue if both frozen, red if both thawed, cyan if “Ref” frozen but not “Obs”, and magenta if “Ref” thawed but not “Obs”.

The F/T surface state signal at sub-boreal latitudes has not such a strong signature as compared to e.g. Arctic areas, which of course have a much colder and longer Winter season [76,77]. The STA could improve detection capability relative to the ERA5-Land and SMAP datasets when the difference between Γ_{fr} and Γ_{th} is greater. Thus, only the smallest and largest 5 data samples are used to set the Γ references. The use of a larger number of measurements to compute Γ_{fr} and Γ_{th} could be reasonable for e.g. Arctic areas because of the colder and larger Winter period. It is recommended to test this with data from future high-inclination GNSS-R missions [77,78].

Two threshold levels T_{fr} and T_{th} are then defined such that the surface state is frozen if $\Delta(t) > T_{fr}$, while the surface state is thawed if $\Delta(t) < T_{th}$. The threshold levels T_{fr} and T_{th} can be varied parametrically to define the Receiver Operating Characteristic (ROC) freeze and thaw curves, using the F/T surface state derived from ERA5-Land temperatures as the reference. A ROC curve shows the capability of diagnosis of a binary classifier as a function of the selected system-threshold. Fig. 6 shows the ROC curves for the “highest” and “high” freeze & thaw confidence levels for July and November. It is found that the sensitivity is improved for

Table I. Statistics of the yearly evolution of CYGNSS F/T detection capabilities corresponding to the “highest” confidence areas.

	January	February	March	April	May	June
Freeze detected	0 %	0 %	0 %	0 %	0 %	9 %
Freeze missed detection	0 %	0 %	0 %	0 %	0 %	27 %
Thaw detected	100 %	100 %	100 %	100 %	100 %	55 %
Thaw missed detection	0 %	0 %	0 %	0 %	0 %	9 %
	July	August	September	October	November	December
Freeze detected	42 %	33 %	26 %	10 %	2 %	0 %
Freeze missed detection	7 %	37 %	4 %	2 %	1 %	0 %
Thaw detected	37 %	14 %	55 %	54 %	72 %	100 %
Thaw missed detection	15 %	16 %	18 %	33 %	29 %	0 %

the “highest” confidence case, so this is the confidence level used hereafter. This improvement is higher in July because of the stronger temperature gradient in the target area as compared to November. Optimum operating points of the ROC freeze and thaw curves are selected as the inflection points where the slope of the curve transitions from >1 to <1 . This is the point beyond which more false than true positives are detected.

The retrieval algorithm is validated for July (Figs. 7a-c) and November (Figs. 7d-f). The reference F/T surface state shown is the “highest” confidence case, and the observed F/T state also corresponds to this case. Frozen areas are depicted in blue, while thawed areas in red (Figs. 7a,b,d,e). Figs. 7c,f show the difference between reference and observed maps. Each pixel is associated to one of the following states:

- Freeze detected \Rightarrow both maps show F (blue)
- Freeze missed detection \Rightarrow reference shows F but retrieval does not (cyan)
- Thaw detected \Rightarrow both maps show T (red)
- Thaw missed detection \Rightarrow reference shows T but retrieval does not (magenta)

The freeze and thaw detections cover most of the “highest” confidence areas, both in July and November. The freeze missed detection is rather low [July $\sim 7\%$, November $\sim 1\%$], however the thaw missed detection pixels are non-negligible [July $\sim 15\%$, November $\sim 29\%$], (Table I). They are identified in the boundary with areas of “moderate” and “low” confidence. Overall, the agreement between the CYGNSS and ERA5-Land F/T surface state maps is high.

V. RESULTS

A. Yearly Evolution of CYGNSS F/T Detection Capabilities

The retrieval algorithm was validated in the previous Section using two specific months, which are representative of different climatological conditions in the target area. On the other hand, the overall main objective in this Section is to evaluate the yearly evolution of F/T surface state detection using ERA5-Land F/T reference maps (Fig. 8), CYGNSS F/T observation maps (Fig. 9), and CYGNSS / ERA5-Land difference F/T maps (Fig. 10, Table I). All these maps correspond to the “highest” confidence level.

Figure 8 provides a graphical description of the monthly reference F/T surface state in the first layer of the soil (0-7 cm) along the year, which is useful for the interpretation of the results. During Summer, the “highest” confidence level areas appear only for thaw conditions. In Autumn, there is a decreasing extension of the thawed areas from April to June. This is consistent with the expected transition towards the coldest period of the year, in the Southern hemisphere. In Winter, the frozen surface is extended along almost all the Andes (Fig. 1). Some areas remain thawed over the Pampas, which provides an adequate scenario to evaluate the STA algorithm. Finally, the extension of frozen areas gradually decreases in Spring, with a remaining frozen area in November. On the other hand, the extension of thawed areas increases with gradually warmer temperatures as we are closer to Summer. Overall, this target area offers a rich scenario with a wide variety of climates and transitions from frozen to thawed and vice-versa.

Figure 9 shows monthly CYGNSS observed F/T surface state maps along the year. Over the Andes, the extension of frozen soil clearly increases from June to August, and it gradually decreases from September to November. On the other hand, the extension of the thawed soil is clearly larger in Summer, rather residual in Winter, and it is transitional in Spring and Summer.

Figure 10 provides the difference between the F/T maps observed by CYGNSS and those derived from ERA5-Land. In June, the freeze missed detection is $\sim 27\%$. ERA5-Land map

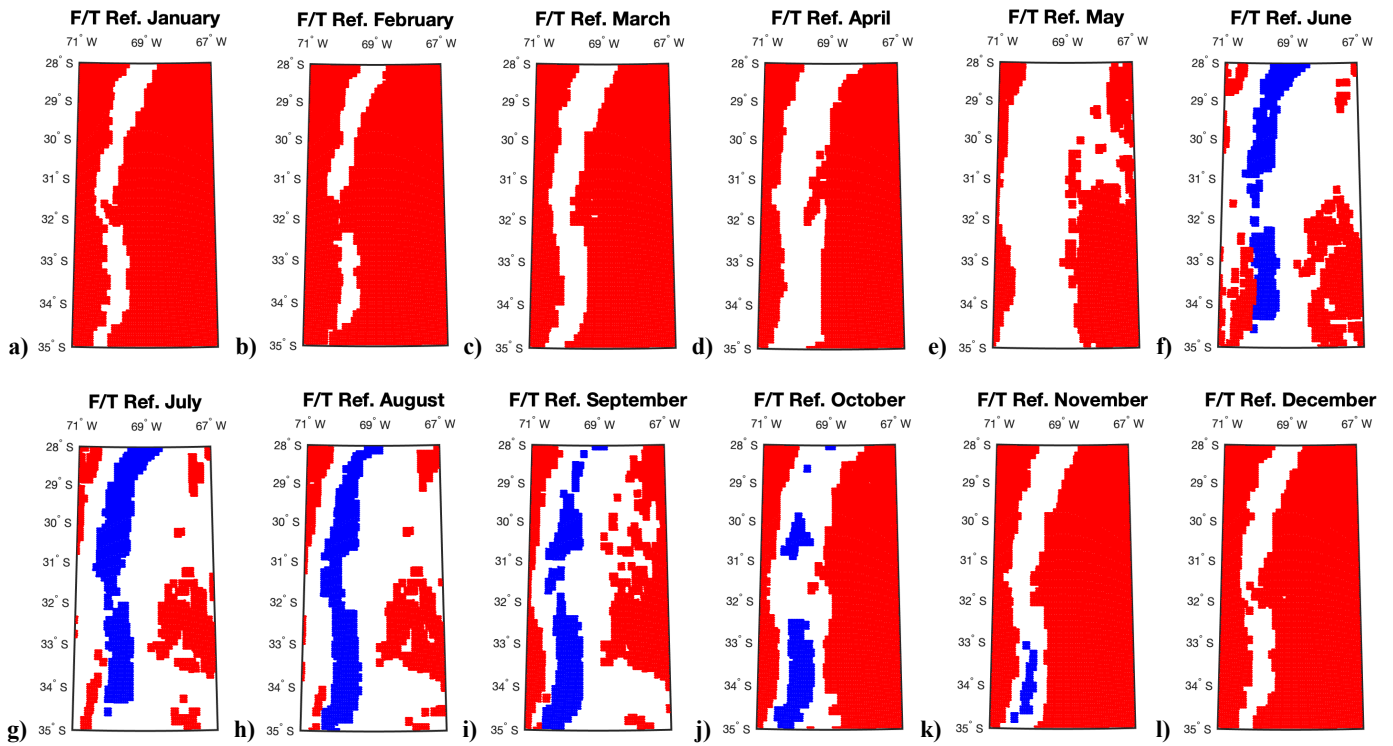


Fig. 8. “Highest” confidence F/T state reference maps for each month, derived from ERA5-Land soil temperatures. Blue-Freeze/Red-Thaw.

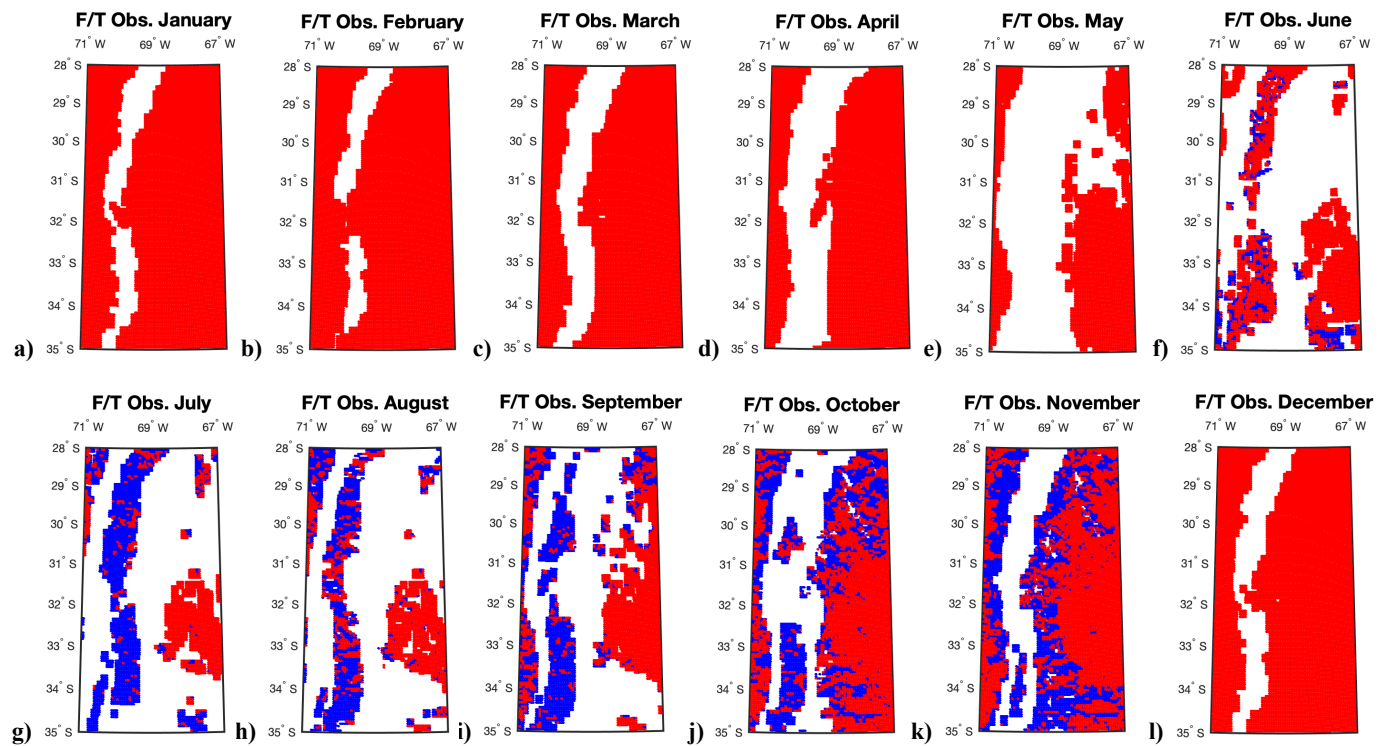


Fig. 9. “Highest” confidence F/T state observed maps for each month, derived from CYGNSS. Blue-Freeze/Red-Thaw.

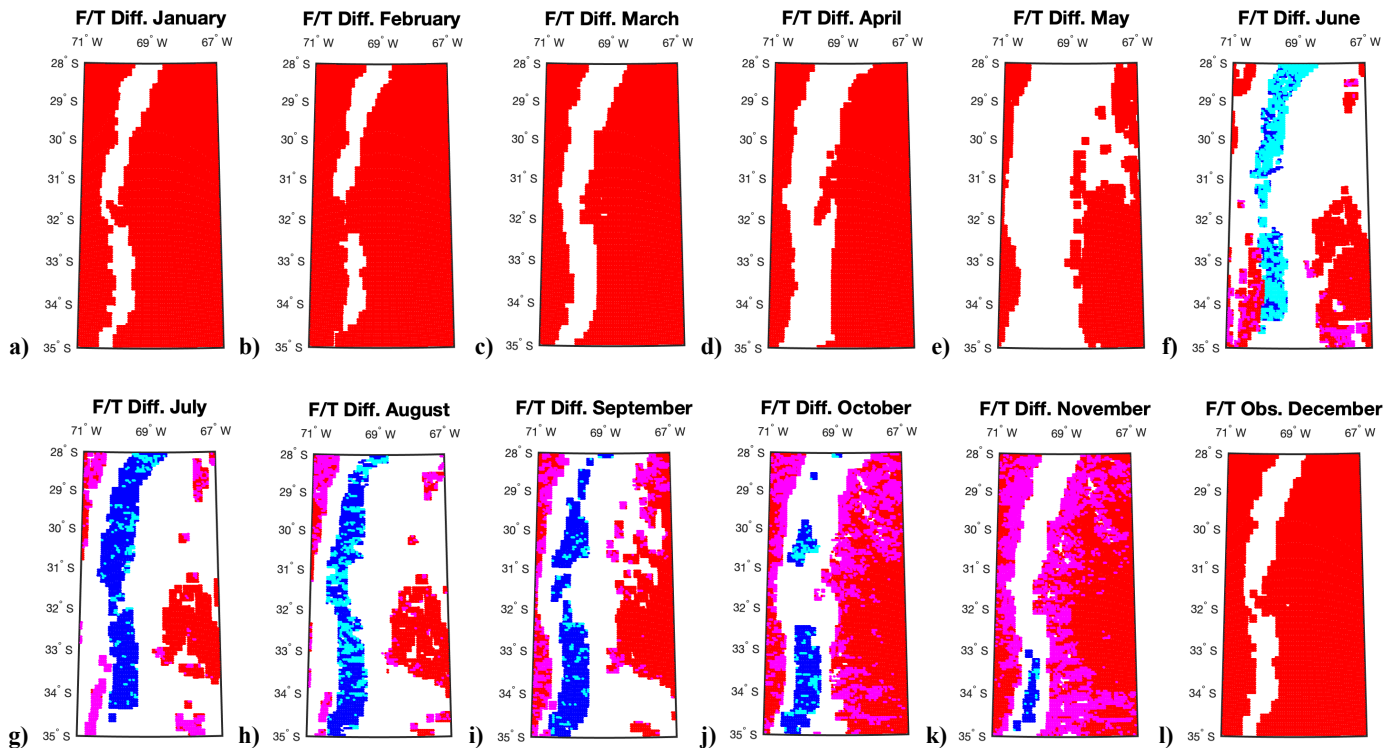


Fig. 10. Difference between CYGNSS observed and ERA5-Land reference F/T maps for each month, using the “highest” confidence level of the reference freeze and thaw state. Freeze detected \Rightarrow both maps show F (blue). Freeze missed detection \Rightarrow reference shows F but retrieval does not (cyan). Thaw detected \Rightarrow both maps show T (red). Thaw missed detection \Rightarrow reference shows T but retrieval does not (magenta).

(Fig. 8f) shows that the surface is frozen over the Andes, however the STA algorithm is identifying the surface as mostly thawed (Fig. 9f). In July, August, and September, the situation is quite different. Both reference and observed F/T maps (Figs. 8g-i and Figs. 9g-i) are rather similar. This is probably because the ERA5-Land temperature is not so accurate in June, since this is a transitional month. A similar situation is found in October (Fig. 8j and Fig. 9j) and November (Fig. 8k and Fig. 9k), but for the thaw missed detection case. The thaw missed detection during October and November is high and roughly similar in both months, $\sim 33\%$ and 29% respectively. There is no evidence of influence of SMC in this observation (Figs. 5 and 10). In the boundary with the “moderate” and “low” confidence thawed areas, CYGNSS detects the soil as frozen while ERA5-Land maps show that the surface temperature is above 0°C . It is assumed that the ERA5-Land temperatures are not so accurate during these periods because the differences appear over the transitional months (Spring and Autumn). Future activities should include ground truth stations to elucidate what is the truth. However, the access to most of these regions is quite complicated because they are high-altitude mountain terrain.

Finally, it is worth to comment that this study uses low incidence angles in the range $\theta_i = [0, 50]^{\circ}$. In this range the impact of the incidence angle on the reflection coefficient can be assumed to be negligible [42]. Additionally, data are

averaged month-by-month at grid cells $\sim 0.05^{\circ}$ by 0.05° . This strategy helps to homogenize data for the study, and to minimize the potential impact of the local terrain slopes.

B. Comparison between CYGNSS and SMAP F/T Surface State Maps

An inter-comparison of CYGNSS observed F/T surface state maps with the SMAP-radiometer F/T product is provided over the “highest” confidence areas for two representative months: February and August. The overall objective is to evaluate the performance of the new CYGNSS F/T capabilities with the more classical L-band microwave radiometry approach, which may provide a higher performance because of the lower impact of surface roughness. Fig. 11 shows a monthly-averaged F/T product derived from the SMAP baseline seasonal threshold algorithm applied to the Normalized Polarization Ratio (NPR) of radiometer measurements [53]. This monthly product reports the state as frozen if any SMAP sample within the month is frozen. In other words, Figs. 11a,d correspond to “peak-detection” maps. Thawed areas are depicted in red and frozen areas in blue, similar to the previous F/T maps. Added to the figure are the corresponding maps produced by ERA5-Land (from Fig. 8) and CYGNSS (from Fig. 9). The surface is totally thawed in February, and frozen areas are properly identified in August over the Andes. This evolution generally agrees with the CYGNSS and the ERA5-Land maps.

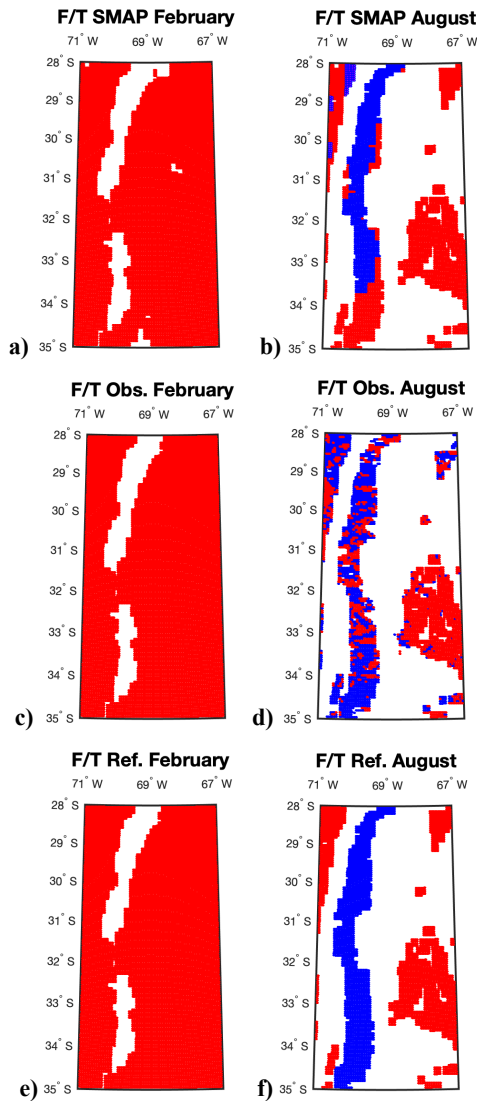


Fig. 11. Comparison between SMAP (a,d), CYGNSS (b,e), and ERA5-Land reference (c,f) F/T products for February (top row) and August (bottom row). Blue-Freeze/Red-Thaw.

C. Time Series Analysis

Two representative target areas are selected over the Andes and the Pampas for a time series analysis along 12 consecutive months from January to December 2019 (Fig. 12). Both target areas correspond to the “highest” confidence level. The objective is to further evaluate the behavior of the F/T detection capability of the algorithm over time. To do so, the scale factor $\Delta(t)$ is selected, which is the main observable used in the retrieval algorithm.

Over the Andes (Fig. 12a), $\Delta(t)$ shows a significant increment from May $\Delta(t) \sim 0.2$ to August $\Delta(t) \sim 1.2$ due to the arrival of the Winter. In Spring, it decreases down to $\Delta(t) \sim 0.8$, as it is expected because of the higher surface temperatures. In Summer, it shows lower values, which correspond to a totally thawed surface. In the Pampas (Fig 12b) on the other hand, $\Delta(t)$ remains fairly low throughout the year. This is consistent with the generally thawed state of the land surface at the location in the Pampas considered.

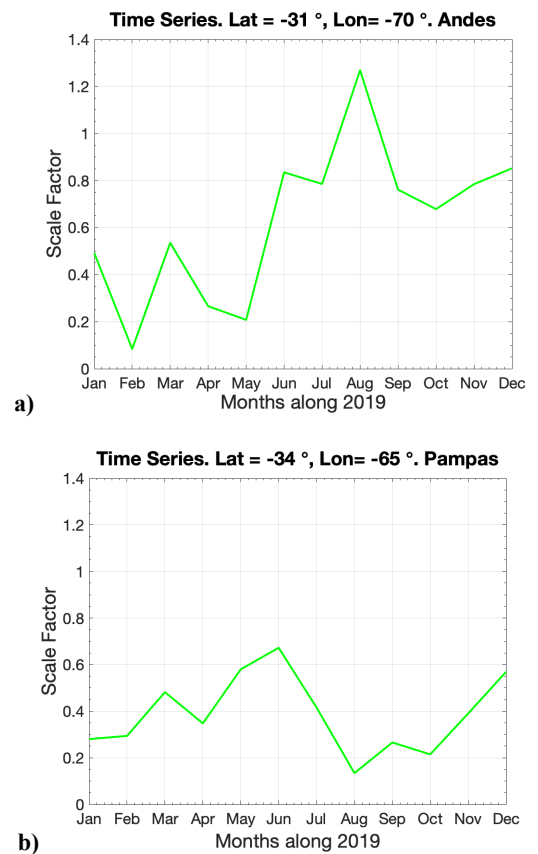


Fig. 12. Time series of the scale factor over two representative target areas in the Andes and the Pampas.

VI. CONCLUSIONS

This paper describes a CYGNSS-based F/T surface state specifically designed STA, which is developed and validated over a target area in South America, covering the Andes Mountains and the Argentinian Pampas. Then, the capability to evaluate the monthly evolution of F/T surface state extension is studied, showing an overall good agreement between STA F/T maps with those derived from ECMWF ERA5-Land surface reanalysis data. Finally, an inter-comparison with the SMAP radiometer-based F/T product also shows consistency with CYGNSS F/T maps, over this target area. In the future, the STA could be applied over polar regions using data from new GNSS-R high-inclination satellites. The higher spatio-temporal sampling of GNSS-R as compared to more traditional Remote Sensing techniques could open new insights in monitoring highly dynamic F/T surfaces processes.

APPENDIX

The equivalent “CYGNSS overall quality flag” over land surfaces is used to filter out the data, improving the quality of the observables. If any one of the following flags are set, then `poor_overall_quality` is set: `large_sc_attitude_err`, `black_body_ddm`, `ddmi_reconfigured`, `spacewire_crc_invalid`, `ddm_is_test_pattern`, `channel_idle`, `low_confidence_ddm_noise_floor`, `large_step_noise_floor`,

large_step_lna_temp, *direct_signal_in_ddm,*
low_confidence_gps_eirp_estimate, *rfi_detected,*
brcs_ddm_sp_bin_delay_error,
brcs_ddm_sp_bin_dopp_error, *gps_pvt_sp3_error,*
sp_non_existent_error, *brcs_lut_range_error,*
ant_data_lut_range_error, *bb_framing_error,*
fsw_comp_shift_error, *sc_altitude_out_of_nominal_range,*
anomalous_sampling_period, *invalid_roll_state,*
incorrect_ddmi_antenna_selection, *sp_in_sidelobe,*
fatal_nst_outage, and *low_zenith_ant_gain.*

REFERENCES

- [1] B.P. Selvam, H. Laudon, F. Guillemette, and M. Berggren, "Influence of Soil Frost on the Character and Degradability of Dissolved Organic Carbon in Boreal Forest Soils," *Journal Geophysical Research: Biogeosciences*, vol. 121, no. 3, pp. 829-840, 2016.
- [2] M.L. Goulden, S. Wofsy, J. Harden, S. Trumbore, P. Crill, S. Gower, T. Fries, B. Daube, S. Fan, D. Sutton, A. Bazzaz, and J. Munger, "Sensitivity of Boreal Forest Carbon Balance to Soil Thaw," *Science*, vol. 279, no. 9, pp. 214-217, 1998.
- [3] L. Oygarden, "Rill and Gully Development During an Extreme Winter Runoff Event in Norway," *CATENA*, vol. 50 no. 2-4, pp. 217-242, 2003.
- [4] J.S. Kimball, K.C. McDonald, S. Frolking, and S.W. Running, "Radar Remote Sensing of the Spring Thaw Transition Across a Boreal Landscape," *Remote Sensing of Environment*, vol. 89, no. 2, pp. 163-175, 2004.
- [5] Y. Kim, J.S. Kimball, K. Zhang, and K.C. McDonald, "Satellite Detection of Increasing Northern Hemisphere Non-Frozen Seasons from 1979 to 2008: Implications for Regional Vegetation Growth," *Remote Sensing of Environment*, vol. 121, pp. 472-487, 2012.
- [6] C. Derksen, X. Xu, R.S. Dunbar, A. Colliander, U. Kim, J.S. Kimball, T.A. Black, E. Euskirchen, A. Langlois, M.M. Loranty, P. Marsh, K. Rautiainen, A. Roy, and J. Stephen, "Retrieving Landscape Freeze/Thaw State from Soil Moisture Active Passive (SMAP) Radar and Radiometer Measurements," *Remote Sensing of Environment*, vol. 194, no. 1, pp. 48-62, 2017.
- [7] J. Obua, S. Westermann, A. Bartsch, N. Berdnikov, H.H. Christiansend, A. Dashtserene, R. Delaloyef, B. Elberling, B. Etlzelmüllera, A. Kholodovh, A. Khomutovc, A. Kääba, M.O. Leibmanc, A.G. Lewkowicz, S.K. Pandah, V. Romanovskiy, R.G. Wayk, A. Westergaard-Nielseng, T. Wum, J. Yamkhine, and D. Zoum, "Northern Hemisphere Permafrost Map Based on TTOP Modelling for 2000-2016 at 1 km² Scale," *Earth-Sciences Reviews*, vol. 193, pp. 299-316, 2019.
- [8] J. Mortin, T. Schröder, A.W. Hansen, B. Holt, and K.C. McDonald, "Mapping of Seasonal Freeze-Thaw Transitions Across the Pan-Arctic Land and Sea Ice Domains with Satellite Radar," *Journal Geophysical Research*, vol. 117, pp. C8, C08004, 2012.
- [9] L. Wang, C. Derksen, and R. Brown, "Recent Changes in Pan-Arctic Melt Onset from Satellite Passive Microwave Measurements," *Geophysical Research Letters*, vol. 40, no. 3, pp. 522-528, 2013.
- [10] J.S. Kimball, K.C. McDonald, A. Keyser, S. Frolking, and S. Running, "Application of the NASA Scatterometer (NSCAT) for Classifying the Daily Frozen and Non-Frozen Landscape of Alaska," *Remote Sensing of Environment*, vol. 75, no. 1, pp. 113-126, 2001.
- [11] A. Colliander, K.C. McDonald, R. Zimmermann, R. Schroeder, J. Kimball, and G. Njoku, "Application of QuikSCAT Backscatter to SMAP Validation Planning: Freeze/Thaw State over ALECTRA Sites in Alaska from 2000 to 2007," *IEEE Transactions on Geosciences and Remote Sensing*, vol. 50, no. 2, pp. 461-468, 2012.
- [12] A. Bartsch, R. Kidd, W. Wagner, and Z. Bartalis, "Temporal and Spatial Variability of the Beginning and End of Daily Spring Freeze/Thaw Cycles Derived from Scatterometer Data," *Remote Sensing of Environment*, vol. 106, no. 3, pp. 360-374, 2007.
- [13] S.M. Bateni, C. Huang, S. Margulis, E. Podest, and K.C. McDonald, "Feasibility of Characterizing Snowpack and the Freeze-Thaw State of Underlying Soil Using Multifrequency Active/Passive Microwave Data," *IEEE Transactions on Geoscience and Remote Sensing*, vol. 51, no. 7, pp. 4085-4102, 2013.
- [14] A. Roy, A. Royer, C. Derksen, L. Brucker, A. Langlois, A. Mialon, and Y. Kerr, "Evaluation of Spaceborne L-band Radiometer Measurements for Terrestrial Freeze/Thaw Retrievals in Canada," *IEEE Journal of Selected Topics in Applied Earth Observations and Remote Sensing*, vol. 8, no. 9, pp. 4442-4459, 2015.
- [15] L. Farhadi, R. Reichle, G. DeLannoy, and J. Kimball, "Assimilation of Freeze-Thaw Observations into the NASA Catchment Land Surface Model," *Journal Hydrometeorology*, vol. 16, no. 2, pp. 730-743, 2015.
- [16] M. Watanabe, G. Kadosaki, Y. Kim, M. Ishikawa, K. Kushida, Y. Sawada, T. Tadono, M. Fukuda, and M. Sato, "Analysis of the Sources of Variation in L-band Backscatter from Terrains with Permafrost," *IEEE Transactions on Geoscience and Remote Sensing*, vol. 50, no. 1, pp. 44-54, 2011.
- [17] M. Schwank, M. Stähli, H. Wydler, J. Leuenberger, C. Mätzler, and H. Flüthler, "Microwave L-band Emission of Freezing Soil," *IEEE Transactions on Geoscience and Remote Sensing*, vol. 42, no. 6, pp. 1252-1261, 2004.
- [18] K. Rautiainen, J. Lemmetyinen, J. Pulliainen, J. Vehviläinen, M. Drusch, A. Kontu, J. Kainulainen, and J. Seppänen, "L-Band Radiometer Observations of Soil Processes in Boreal and Subarctic Environments," *IEEE Transactions on Geoscience and Remote Sensing*, vol. 50, no. 5, pp. 1483-1497, 2012.
- [19] K. Rautiainen, J. Lemmetyinen, M. Schwank, A. Kontu, C. Menard, C. Mätzler, M. Drusch, A. Wiesmann, J. Ikonen, and J. Pulliainen, "Detection of Soil Freezing from L-Band Passive Microwave Observations," *Remote Sensing of Environment*, vol. 147, pp. 206-218, 2014.
- [20] K. Rautiainen, T. Parkkinen, J. Lemmetyinen, M. Schwank, A. Wiesmann, J. Ikonen, C. Derksen, S. Davydov, A. Davydova, J. Boike, M. Langer, M. Drusch, and J. Pulliainen, "SMOS Prototype Algorithm for Detecting Autumn Soil Freezing," *Remote Sensing of Environment*, vol. 180, pp. 346-360, 2016.
- [21] E. Podest, K.C. McDonald, and J. Kimball, "Multisensor Microwave Sensitivity to Freeze/Thaw Dynamics Across a Complex Boreal Landscape," *IEEE Transactions on Geoscience and Remote Sensing*, vol. 52, no. 11, pp. 6818-6828, 2014.
- [22] J. Du, J. Kimball, M. Azarderakhsh, R.S. Dunbar, M. Moghaddam, and K.C. McDonald, "Classification of Alaska Spring Thaw Characteristics Using Satellite L-band Radar Remote Sensing," *IEEE Transactions on Geoscience and Remote Sensing*, vol. 53, no. 1, pp. 542-556, 2014.
- [23] X. Xu, C. Derksen, S. Yueh, R.S. Dunbar, and A. Colliander, "Freeze/Thaw Detection and Validation Using Aquarius L-band Backscattering Data," *IEEE Journal of Selected Topics in Applied Earth Observations and Remote Sensing*, vol. 9, no. 4, pp. 1370-1381, 2016.
- [24] M. Martin-Neira, "A Passive Reflectometry and Interferometry System (PARIS): Application to Ocean Altimetry," *ESA Journal*, vol. 17, no. 9, pp. 331-355, 1993.
- [25] V.U. Zavorotny, and A.G. Voronovich, "Scattering of GPS Signals from the Ocean with Wind Remote Sensing Application," *IEEE Transactions on Geoscience and Remote Sensing*, vol. 38, no. 2, pp. 951-964, 2000.
- [26] J.L. Garrison, A. Komjathy, V.U. Zavorotny, and S.J. Katzberg, "Wind Speed Measurement Using Forward Scattered GPS Signals," *IEEE Transactions on Geoscience and Remote Sensing*, vol. 40, no. 1, pp. 50-65, 2002.
- [27] S.T. Lowe, J.L. LaBrecque, C. Zuffada, L.J. Romans, L.E. Young, and G.A. Hajj, "First Spaceborne Observation of an Earth-Reflected GPS Signal," *Radio Science*, vol. 37, pp. 7-1-7-28, 2002.
- [28] S. Gleason, S. Hodgart, Y. Sun, C. Gommenginger, S. Mackin, M. Adjrard, and M. Unwin, "Detection and Processing of Bistatically Reflected GPS Signals from a Low Earth Orbit for the Purpose of Ocean Remote Sensing," *IEEE Transactions on Geoscience and Remote Sensing*, vol. 43, no. 6, pp. 1229-1241, 2005.
- [29] K.M. Larson, E.E. Small, E. Gutmann, A. Bilich, P. Axelrad, and J. Braun, "Using GPS Multipath to Measure Soil Moisture Fluctuations: Initial Results," *GPS Solutions*, vol. 12, no. 3, pp. 173-177, 2008.
- [30] C.S. Ruf, R. Atlas, P.S. Chang, M.P. Clarizia, J.L. Garrison, S. Gleason, S.J. Katzberg, Z. Jelenak, J.T. Johnson, S.J. Majumdar, A. O'brien, D.J. Posselt, A.J. Ridley, R.J. Rose, and V.U. Zavorotny, "New Ocean Winds Satellite Mission to Probe Hurricanes and Tropical Convection, Bulletin American Meteorological Society," vol. 97, pp. 385-395, 2015.
- [31] R. Shah, X. Xu, S. Yueh, C.S. Chae, K. Elder, B. Starr, and Y. Kim, "Remote Sensing of Snow Water Equivalent Using P-band Coherent Reflection," *IEEE Geoscience Remote Sensing Letters*, vol. 14, no. 3, pp. 309-313, 2019.
- [32] N. Rodriguez-Alvarez, X. Bosch-Lluis, A. Camps, M. Vall-Llossera, E. Valencia, J.F. Marchan-Hernandez, and I. Ramos-Perez, "Soil Moisture Retrieval Using GNSS-R Techniques: Experimental Results over a Bare Soil Field," *Transactions on Geoscience and Remote Sensing*, vol. 47, no. 11, pp. 3616-3624, 2009.
- [33] C. Chew, R. Shah, C. Zuffada, G. Hajj, D. Masters, and A. Mannucci, "Demonstrating Soil Moisture Remote Sensing with Observations from the UK TechDemoSat-1 Satellite Mission," *Geophysical Research Letters*, vol. 43, no. 7, pp. 3317-3324, 2016.
- [34] H. Carreno-Luengo, S.T. Lowe, C. Zuffada, S. Esterhuizen, and S. Oveisgharan, "Spaceborne GNSS-R from the SMAP Mission: First Assessment

- of Polarimetric Scatterometry over Land and Cryosphere,” *MDPI Remote Sensing*, vol. 9, no. 4, pp. 362, 2017.
- [35] H. Carreno-Luengo, G. Luzi, and M. Crosetto, “Sensitivity of CYGNSS Bistatic Reflectivity and SMAP Microwave Radiometry Brightness Temperature to Geophysical Parameters over Land Surfaces,” *IEEE Journal of Selected Topics in Applied Earth Observations and Remote Sensing*, vol. 12, no. 1, pp. 107-122, 2019.
- [36] M. Kurum, M. Deshpande, A.T. Joseph, P.E. O’Neill, R.H. Lang, and O. Eroglu, “SCoBi-Veg: A Generalized Bistatic Scattering Model of Reflectometry from Vegetation for Signals of Opportunity Applications,” *IEEE Transactions on Geoscience and Remote Sensing*, vol. 57, no. 2, pp. 1049-1068, 2018.
- [37] M. Morris, C. Chew, J.T. Reager, R. Shah, and C. Zuffada, “A Novel Approach to Monitoring Wetland Dynamics Using CYGNSS: Everglades Case Study,” *Remote Sensing of Environment*, vol. 233, 2019.
- [38] C. Gerlein-Safdi, and C. Ruf, “A CYGNSS-Based Algorithm for the Detection of Inland Waterbodies,” *Geophysical Research Letters*, vol. 46, no. 21, no. 12065-12072, 2019.
- [39] C. Chew, S.T. Lowe, N. Parazoo, S. Esterhuizen, S. Oveisgharan, E. Podest, C. Zuffada, and A. Freedman, “SMAP Radar Receiver Measures Land Surface Freeze/Thaw State Through Capture of Forward-Scattered L-Band Signals,” *Remote Sensing of Environment*, vol. 198, no. 1, pp. 333-344, 2017.
- [40] D. Comite, L. Cenci, A. Colliander, and N. Pierdicca, “Monitoring Freeze-Thaw State by Means of GNSS Reflectometry: An Analysis of TechDemoSat-1 Data,” *IEEE Journal of Selected Topics in Applied Earth Observations and Remote Sensing*, vol. 13, pp. 2996-3005, 2020.
- [41] X. Wu, Z. Dong, S. Jin, Y. He, Y. Song, W. Ma, and L. Yang, “First Measurement of Soil Freeze/Thaw Cycles in the Tibetan Plateau Using CYGNSS GNSS-R Data,” *MDPI Remote Sensing*, vol. 12, no. 15, pp. 2361, 2020.
- [42] F. Fabra, GNSS-R as a Source of Opportunity for Remote Sensing of the Cryosphere. Ph.D. Thesis, Universitat Politècnica de Catalunya, Barcelona, Spain, 2014.
- [43] F.T. Ulaby, D.G. Long, W. Blackwell, C. Elachi, A. Fung, C. Ruf, K. Sarabandi, H. Zebker, and J. van Zyl, *Microwave Radar and Radiometric Remote Sensing*. Published in the United States of America by The University of Michigan Press, 2014.
- [44] M.T. Hallikainen, “Microwave Dielectric Behavior of Wet Soil-Part I: Empirical Models and Experimental Observations,” *IEEE Transactions on Geoscience and Remote Sensing*, vol. GE-23, no. 1, pp. 25–34, 1985.
- [45] M.C. Dobson, “Microwave Dielectric Behavior of Wet Soil-Part II: Dielectric Mixing Models,” *IEEE Transactions on Geoscience and Remote Sensing*, vol. GE-23, no. 1, pp. 35-46, 1985.
- [46] L. Zhang, J. Shi, and Z. Zhang, “The Estimation of Dielectric Constant of Frozen Soil-Water Mixture at Microwave Bands,” in *Proc. of the 2003 IEEE International Geoscience and Remote Sensing Symposium*, Toulouse, France, 2003, pp. 2903-2905.
- [47] A.P. Gorbunov, “Permafrost Investigations in High-Mountain Regions,” *Arctic and Alpine Research*, vol. 10, no. 2, pp. 283-294, 1978.
- [48] T. Wang, C. Ruf, B. Block, D. McKague, and S. Gleason, “Design and Performance of a GPS Constellation Power Monitor System for Improved CYGNSS L1B Calibration,” *IEEE Journal of Selected Topics in Applied Earth Observation and Remote Sensing*, vol. 12, no. 1, pp. 26-36, 2019.
- [49] T. Wang, C.S. Ruf, S. Gleason, A.J. O’Brien, D.S. McKague, B.P. Block, and A. Russel “Dynamic Calibration of GPS Effective Isotropic Radiated Power for GNSS-Reflectometry Earth Remote Sensing,” *IEEE Transactions on Geoscience and Remote Sensing*, 2021. DOI: 10.1109/TGRS.2021.3070238.
- [50] CYGNSS, 2020. CYGNSS Level 1 (L1) data from the version 3.0 (v3.0) Science Data Record. Dataset accessed at <https://podaac.jpl.nasa.gov/>
- [51] ECMWF, 2020. ECMWF ERA5-Land hourly data. Dataset accessed at <https://cds.climate.copernicus.eu/cdsapp#!/dataset/10.24381/cds.e2161bac?tab=overview>
- [52] Y.H. Kerr, P. Waldteufel, J.P. Wigneron, S. Delwart, F. Cabot, J. Boutin, M.J. Escorihuela, J. Font, N. Reul, C. Gruhier, S.E. Juglea, M.R. Drinkwater, A. Hahne, M. Martin-Neira, and S. Mecklenburg, “The SMOS Mission: New Tool for Monitoring Key Elements of the Global Water Cycle,” in *Proc. of the IEEE International Geoscience and Remote Sensing Symposium*, Honolulu, Hawaii, 2010, pp. 666-687.
- [53] S. Dunbar, X. Xu, A. Colliander, C. Derksen, J. Kimball and Y. Kim, August 2020. Algorithm Theoretical Basis Document (ATBD) SMAP Level 3 Radiometer Freeze/Thaw Data Products (L3_FT_P and L3_FT_P_E), California Institute of Technology.
- [54] M.P. Clarizia, C. Ruf, P. Cipollini, and C. Zuffada, “First Spaceborne Observation of Sea Surface Height Using GPS-Reflectometry,” *AGU Geophysical Research Letters*, vol. 43, pp. 767-774, 2016.
- [55] A. Camps, H. Park, M. Pablos, G. Foti, C.P. Gommenginger, P.W. Liu, and J. Judge, “Sensitivity of GNSS-R Spaceborne Observations to Soil Moisture and Vegetation,” *IEEE Journal of Selected Topics in Applied Earth Observations and Remote Sensing*, vol. 9, no. 10, pp. 4730-4732, 2016.
- [56] C. Chew, and E. Small, “Soil Moisture Sensing Using Spaceborne GNSS Reflections: Comparison of CYGNSS Reflectivity to SMAP Soil Moisture,” *AGU Geophysical Research Letters*, vol. 45, no. 9, pp. 4049-4057, 2018.
- [57] M.P. Clarizia, N. Pierdicca, F. Constantini, and N. Floury, “Analysis of CYGNSS Data for Soil Moisture Retrieval,” *IEEE Journal Selected Topics in Applied Earth Observations and Remote Sensing*, vol. 12, no. 7, pp. 2227-2235, 2019.
- [58] E. Loria, A. O’Brien, and I.J. Gupta, “Detection and Separation of Coherent Reflections in GNSS-R Measurements Using CYGNSS Data,” in *Proc. of the IEEE International Geoscience and Remote Sensing Symposium*, Valencia, Spain, 2018, pp. 3995-3998.
- [59] Y. Wang and Y. Morton, “Coherent GNSS Reflection Signal Processing for High-Precision and High-Resolution Spaceborne Applications,” *IEEE Transactions on Geoscience and Remote Sensing*, vol. 59, no.1, pp. 831-842, 2021.
- [60] E. Loria, A. O’Brien, V. Zavorotny, B. Downs and C. Zuffada, “Analysis of Scattering Characteristics from Inland Bodies of Water Observed by CYGNSS,” *Remote Sensing of Environment*, vol. 254, 2020.
- [61] A. Egido, S. Paloscia, E. Motte, L. Guerriero, N. Pierdicca, M. Caparrini, E. Santi, G. Fontanelli, and N. Floury, “Airborne GNSS-R Polarimetric Measurements for Soil Moisture and Above-Ground Biomass Estimation,” *IEEE Journal of Selected Topics in Applied Earth Observations and Remote Sensing*, vol. 7, no. 5, pp. 1522-1532, 2014.
- [62] S. Gleason, A. O’Brien, A. Russel, M.M. Al-Khaldi and J.T. Johnson, “Geolocation, Calibration and Surface Resolution of Spaceborne GNSS-R Land Observations,” *Remote Sensing*, vol. 12, no. 8, pp. 1317, 2020.
- [63] A.M. Balakhder, M.M. Al-Khaldi, and J. Johnson, “On the Coherency of Ocean and Land Surface Specular Scattering for GNSS-R and Signals of Opportunity Systems,” *IEEE Transactions on Geoscience and Remote Sensing*, vol. 57, no. 12, pp. 10426-10436, 2019.
- [64] M.M. Al-Khaldi, J.T. Johnson, S. Gleason, E. Loria, A.J. O’Brien, and Y. Yi, “An Algorithm for Detecting Coherence in Cyclone Global Navigation Satellite System Mission Level 1 Delay Doppler Maps,” *IEEE Transactions on Geoscience and Remote Sensing*, vol. 59, no. 5, pp. 4454-4463, 2021.
- [65] M.M. Al-Khaldi, J.T. Johnson, S. Gleason, C. Chew, C. Safdi, R. Shah, and C. Zuffada, “Inland Water Body Mapping Using CYGNSS Coherence Detection,” *IEEE Transactions on Geoscience and Remote Sensing*, 2021.
- [66] M.M. Al-Khaldi, R. Shah, C.C. Chew, J.T. Johnson and S. Gleason, “Mapping the Dynamics of the South Asian Monsoon Using CYGNSS’s Level-1 Signal Coherency,” *IEEE Journal of Selected Topics in Applied Earth Observations and Remote Sensing*, 2020.
- [67] D. Comite and N. Pierdicca. “Decorrelation of the Near-Specular Land Scattering in Bistatic Radar Systems,” *IEEE Transactions on Geoscience and Remote Sensing*, 2021.
- [68] N. Pierdicca, L. Guerriero, R. Giusto, M. Brogioni, and A. Egido, “SAVERS: A Simulator of GNSS Reflections from Bare and Vegetated Soils,” *IEEE Transactions on Geoscience and Remote Sensing*, vol. 52, no. 10, pp. 6542-6554, 2014.
- [69] D. Comite, F. Ticconi, L. Dente, L. Guerriero, and N. Pierdicca, “Bistatic Coherent Scattering from Rough Soils with Application to GNSS Reflectometry,” *IEEE Transactions on Geoscience and Remote Sensing*, vol. 58, no.1, pp. 612 - 625, 2019.
- [70] L. Dente, L. Guerriero, D. Comite, and N. Pierdicca, “Space-Borne GNSS-R Signal Over a Complex Topography: Modeling and Validation,” *IEEE Journal of Selected Topics in Applied Earth Observation and Remote Sensing*, vol. 13, pp. 1218-1213, 2020.
- [71] D. Comite and N. Pierdicca, “Decorrelation of the Near-Specular Land Scattering in Bistatic Radar Systems,” *IEEE Transactions on Geoscience and Remote Sensing*, 2021, DOI: 10.1109/TGRS.2021.3072864.
- [72] H. Carreno-Luengo, G. Luzi, and M. Crosetto, “Above-Ground Biomass Retrieval over Tropical Forests: a Novel GNSS-R Approach with CYGNSS,” *MDPI Remote Sensing*, vol. 12, no. 9, pp. 1368, 2020.
- [73] H. Carreno-Luengo, G. Luzi, and M. Crosetto, “First Evaluation of Topography on GNSS-R: an Empirical Study Based on a Digital Elevation Model,” *MDPI Remote Sensing*, vol. 11, no. 21, pp. 2556, 2019.
- [74] G. Foti, C. Gommenginger, M. Unwin, P. Jales, J. Tye, and J. Rosello, “An Assessment of Non-geophysical Effects in Spaceborne GNSS Reflectometry Data from the UK TechDemoSat-1 Mission,” *IEEE Journal of Selected Topics in Applied Earth Observations and Remote Sensing*, vol. 10, no. 7, pp. 3418-3429, 2017.

- [75] C. Hu, C. Benson, H. Park, A. Camps, L. Qiao, and C. Rizos, "Detecting Targets Above the Earth's Surface Using GNSS-R Delay Doppler Maps: Results from TDS-1," *MDPI Remote Sensing*, vol. 11, no.19, pp. 2327, 2019.
- [76] S. Kraatz, J.M. Jacobs, R. Schröder, E. Cho, M. Cosh, M. Seyfried, J. Prueger, and S. Livingston, "Evaluation of SMAP Freeze/Thaw Retrieval Accuracy at Core Validation Sites in the Contiguous United States," *MDPI Remote Sensing*, vol. 10, no. 9, pp. 1483, 2018.
- [77] K. Rautiainen, D. Comite, J. Cohen, M. Unwin, and N. Pierdicca, "GNSS-Reflected Signals for Permafrost Monitoring," in *Proc. of the IEEE International Geoscience and Remote Sensing Symposium, Brussels, Belgium, 2021*, pp. 140-143.
- [78] M. Unwin, N. Pierdicca, E. Cardellach, K. Rautiainen, G. Foti, P. Blunt, L. Guerriero, E. Santi, and M. Tossaint, "An Introduction to the HydroGNSS GNSS Reflectometry Remote Sensing Mission", *IEEE Journal Selected Topics in Applied Earth Observations and Remote Sensing*, 2021, DOI: 10.1109/JSTARS.2021.3089550.